INTERNATIONAL JOURNAL FOR NUMERICAL METHODS IN FLUIDS
*Int. J. Numer. Meth. Fluids* 2008; **56**:2179–2205
Published online 25 October 2007 in Wiley InterScience (www.interscience.wiley.com). DOI: 10.1002/fld.1613

# A robust methodology for RANS simulations of highly underexpanded jets

G. Lehnasch[1, ‡] and P. Bruel[2, *, †]

[1]*CNRS and Université de Poitiers Laboratoire d'Études Aérodynamiques, UMR 6609 43 Rue de l'Aérodrome, 86036 Poitiers Cedex, France*
[2]*CNRS and Université de Pau et des Pays de l'Adour Laboratoire de Mathématiques et de leurs Applications, UMR 5142 64013 Pau, France*

SUMMARY

This work aims at developing/combining numerical tools adapted to the simulation of the near field of highly underexpanded jets. An overview of the challenging numerical problems related to the complex shock/expansion structure encountered in these flows is given and an efficient and low-cost numerical strategy is proposed to overcome these, even on short computational domains. Based on common upwinding algorithms used on unstructured meshes in a mixed finite-volume/finite-element approach, it relies on an appropriate utilization of zonal anisotropic remeshing algorithms. This methodology is validated for the whole near field of cold air jets issuing from axisymmetric convergent nozzles and yielding various underexpansion ratios. In addition, the most usual corrections of the $k$–$\varepsilon$ model used to take into account the compressibility effects on turbulence are precisely assessed. Copyright © 2007 John Wiley & Sons, Ltd.

Received 13 March 2007; Revised 31 July 2007; Accepted 1 August 2007

KEY WORDS: underexpanded jets; shocks; compressible turbulence; mesh adaptation; finite element/finite volume

## 1. INTRODUCTION

The key parameter used to classify the various morphologies of an axisymmetric underexpanded jet which discharges into a quiescent atmosphere is the nozzle pressure ratio (NPR) between the static pressures prevailing at the nozzle exit and in the surrounding atmosphere. For small NPRs (typically between 1 and 2.1 for an air flow), the initial expansion waves reflect at the jet boundary, coalesce and give rise to an oblique shock regularly reflecting at the jet axis. Due

*Correspondence to: P. Bruel, Laboratoire de Mathématiques et de leurs Applications, UMR 5142 CNRS-UPPA, Avenue de l'Université, BP 1155, 64013 Pau Cedex, France.
†E-mail: pascal.bruel@univ-pau.fr
‡E-mail: guillaume.lehnasch@lea.univ-poitiers.fr

to the new expansion zone appearing downstream of the reflected shock, this first shock cell structure is replicated several times until the growing shear layer reaches the jet axis. Thus, weakly underexpanded jets yield the famous diamond-like shock structure embedded within the potential core. Such jets are used in many applications, for instance to assist laser cutting [1], to drill by thermal spallation [2] or to improve surface coating by thermal sprays [3]. They are also the subject of some recent studies whose objectives, among others, are to reduce the screech noise [4] or the infrared signature in rocket exhaust plumes [5]. For higher values of NPR, the shock structure becomes more complex, as illustrated in Figure 1 (for NPR typically larger than 10). Indeed, the reflection of the incident shock (zone 1) at the axis cannot be regular anymore, so that a strong shock, called a Mach disk (zone 2), appears. The flow is subsonic downstream of this Mach disk, whereas it remains supersonic downstream of the reflected shock (zone 3). The triple point connects the various discontinuities and is at the origin of a new slip line, rapidly evolving into a shear layer, which separates these two flows embedded within the potential core. The lengths of the first shock cell and of the subsonic zone are increasing functions of NPR, and so is the shock diameter. As a consequence, typically for about NPR$>$4, the subsonic zone drills the second structure and 'swallows' all the following structures for NPR$>$7. In such a case, the jet yields a highly curved shock structure (the 'barrel shock'), followed by two distinct coaxial shear layers wherein expansion and compression zones alternate without giving rise to any additional stationary shock structure. For NPR$>$10, the first shock cell is so large that the Mach disk directly interacts with the main shear layer. Unfortunately, very little experimental data are available to describe such interactions. Correlations are available though to approximately determine the distance $X_{\mathrm{dm}}$ between the Mach disk position and the orifice section [6, 7], the Mach disk diameter $D_{\mathrm{dm}}$ [8] or the length $L_{\mathrm{s}}$ of the subsonic core [9]. In addition, experimental data such as those of Love *et al.* [10] can be used to determine the initial angle $a_i$ between the jet boundary and the axis. However, neither correlations nor experimental data are yet available to describe the evolution of the Mach disk curvature or the angle $a_r$ between the reflected shock and the axis which are among the key parameters controlling the mixing properties of the jet downstream of the Mach disk. The high levels of shock curvature encountered for these highly underexpanded jets also play an important role in (i) the modification of the turbulence structure in comparison with perfectly expanded jets; (ii) the instabilities related to the strong interaction between the Mach disk and the shear layer; and (iii) the enhancement of the development of streamwise vortices surrounding the near-jet core [11] (induced by Taylor–Görtler instabilities). Nevertheless, their impact on the turbulent mixing properties is not clearly identified. So, a better understanding of the various aspects of the structure of such flows is necessary to improve the safety and the efficiency of the various applications where they are encountered. For instance, (i) in short take off and vertical landing situations [12], the greatly enhanced air entrainment is likely to induce severe thrust losses while the large amplitude of instabilities can severely damage the nozzle lip or (ii) during the certification procedure of a newly developed jet engine, the manufacturer has to ensure the preservation of the engine integrity, in the case of an accidental boring of the chamber wall, in spite of the formation of a high-pressure jet, possibly reacting, which can impact and severely damage vital equipments (in particular, the pylon truss that attaches the engine block to the plane wing). Considering the difficulty of experimentally investigating such flows with state-of-the-art metrology, numerical simulations are an extremely useful tool that can be of great help in improving our knowledge of the detailed structure of these flows and of the interaction with their environment in many situations of practical interest.

Unfortunately, due to the great complexity and sensitivity of the flow structure to the value of NPR, the development of a modeling and numerical strategy able to cope with this kind of flow



DOI: 10.1002/fld

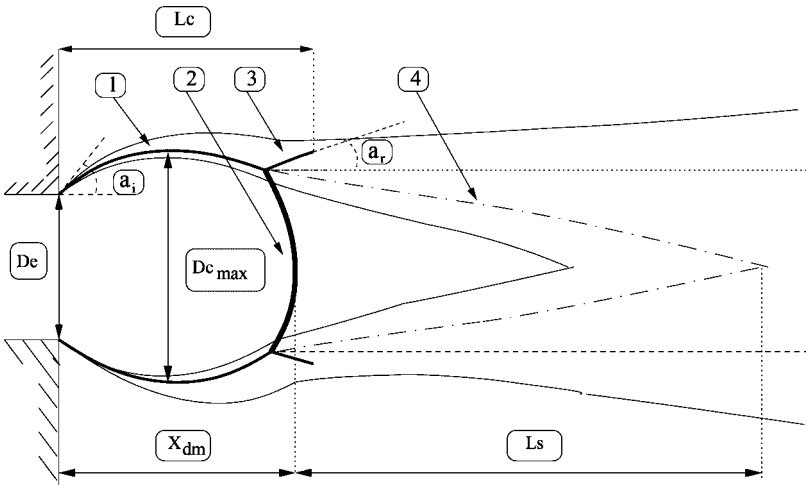


Figure 1. Schematic of the near-field structure of a highly underexpanded jet for NPR>10: (1) incident shock, (2) Mach disk, (3) reflected shock, (4) sonic line, ($D_e$) orifice diameter, ($a_i$) initial angle between the shock and the axial direction, ($a_r$) angle between the reflected shock and the axial direction, ($D_{\mathrm{dm}}$) Mach disk diameter, ($Dc_{\max}$) maximal radial extension of the shock structure, ($X_{\mathrm{dm}}$) length of the shock structure, ($L_{\mathrm{s}}$) length of the subsonic zone.

while preserving a good robustness and fair accuracy over a wide range of NPR is not an easy task. To begin with moderately underexpanded turbulent jets, the pioneering studies of Dash and Wolf [13, 14] are a good example of what can be achieved by considering a two-dimensional flow configuration. By using a two-equation model for a one-point turbulence closure ($k$–$\varepsilon$ and $k$–$\omega$ models) and by modifying only the expression of the turbulent viscosity coefficient in order to correctly reproduce the observed spreading rate of supersonic shear layers, these authors obtained some promising results. A similar approach was followed by Chuech *et al.* [15] in the case of an axisymmetric configuration. But in spite of these promising results, the model was not able to precisely capture the complex interactions occurring within the potential zone. Continuing now with highly underexpanded jets, Cumber *et al.* [16, 17] showed, for various levels of NPR, that the compressibility correction of Sarkar *et al.* [18] greatly improved the quality of the prediction of the axial velocity evolution, but only in the far flow field. By modifying the standard model constant $C_{\varepsilon 2}$ and using a new scale for the axial coordinate to take into account a reduced effective nozzle diameter (the boundary layer not being calculated), they showed that the error on the predicted shock locations could be reduced. However, a great amplitude error of the axial velocity or pressure still remained. In fact, whereas the standard $k$–$\varepsilon$ model leads to an overestimation of the spreading rate of the shear layer, this compressibility correction leads to an opposite effect accompanied by an underestimation of the level of the axially decaying oscillations of the physical variables within the potential core. Such tendencies have been recently confirmed by Birkby and Page [19]. Abdol-Hamid and Wilmoth [20] have attempted to consider some non-equilibrium turbulence effects in addition to the compressibility corrections. According to these authors, a multiscale approach could greatly help to more accurately describe the modification of the turbulence structure related, in particular, to the interaction of the first reflected shock with the shear layer. Unfortunately, the determination of the related transfer coefficients is a delicate task that would benefit from



DOI: 10.1002/fld

specifically dedicated experiments not yet available. This situation can explain why such an approach has not yet led to any further developments. Focusing now on the numerical strategies elaborated to deal with these jets, it should be emphasized that meshing and mesh adaptation procedures used for most simulations of these particular turbulent flows (see, for example, the study by Prudhomme and Haj-Hariri [21]) are not reported to be extensively based on parameters related both to some crucial flow properties (steep gradients and/or curvatures associated to the spatial evolution of the various variables) and to CFD-related constraints (control volume geometrical aspect ratio for instance). Considering the complexity of the flow morphology, a careful mesh adaptation [12] seems though to be unavoidable to obtain reasonably mesh-independent results. For example, Berzins *et al.* [22] applied a h-refinement strategy for adapting the mesh for simulating underexpanded jets with an NPR up to about 16. Their approach was based on a local error estimate calculated from the difference between the solution obtained by using a first-order spatial discretization and a second one. However, the comparisons with experimental data have been quite limited in most of these studies since they have been confined to a scrutinization of the variables' evolution on the jet axis only. As a consequence, the origins of the reported numerical inaccuracy are not yet clearly identified for highly underexpanded jets since it was not easy to determine the respective importance of the possible sources of uncertainty, e.g. the intrinsic weaknesses of the physical modeling and those of the numerical scheme employed. Last but not least, to the best of our knowledge and for NPRs larger than 5, there exists no detailed numerical study focusing on the near flow field in an axisymmetric configuration, although this zone is of paramount importance as far as the subsequent development of the jet is concerned. Accordingly, the primary objective of the present study is to propose a relevant combination of mature turbulence modeling and numerical techniques able to ensure both robustness and fair accuracy of the simulations of the near field of underexpanded jets over a wide range of NPR. A methodology of mesh embedding/adaptation aimed at shortening as much as possible the streamwise extension of the computational domain while preserving the accuracy of the numerical procedure in the zone of primary interest, e.g. in the near flow field, is presented. Various corrections of the $k$–$\varepsilon$ turbulence model proposed in the literature to incorporate compressibility effects are then tested in the case of a perfectly expanded jet, considered to be the first step of a model testing before considering its use for the simulation of highly underexpanded turbulent jets. Namely, if the compressibility corrections fail to improve the quality of the results for a perfectly expanded jet, it is highly doubtful that they will do so when simulating highly underexpanded jets. Finally, comparisons with recently available experimental data illustrate the level of accuracy that can be achieved with such a methodology whilst opening a perspective of clear assessment of any (potential) gain in accuracy that could be obtained in the future through turbulence modeling and/or numerical procedure evolutions.

## 2. MODELING AND NUMERICAL FRAMEWORK

### 2.1. *Basis of flow description*

In the axisymmetric coordinate system $(O, x, r)$, the conservative form of the averaged compressible Navier–Stokes equations is considered to describe the temporal and spatial evolution of the vector of conservative variables $U = (\overline{\rho}, \overline{\rho}\tilde{v}_x, \overline{\rho}\tilde{v}_r, \overline{\rho}\tilde{E})^{\mathrm{T}}$, where $\rho$, $v_x$, $v_r$ and $E$ stand for the density, the longitudinal and radial velocity components and the total energy (including the turbulence kinetic energy), respectively. Adopting standard notations, the overbar denotes a Reynolds average



DOI: 10.1002/fld

and the tilde a Favre (e.g. density weighted) average. This set of governing equations can be cast in the following compact form:

$$\frac{\partial}{\partial t}\mathbf{U}+\frac{\partial}{\partial x}\mathbf{F}_x(\mathbf{U})+\frac{\partial}{\partial r}\mathbf{F}_r(\mathbf{U})=\frac{\partial}{\partial x}\mathbf{D}_x(\mathbf{U})+\frac{\partial}{\partial r}\mathbf{D}_r(\mathbf{U})+\mathbf{S}_e(\mathbf{U})+\mathbf{S}_v(\mathbf{U}) \tag{1}$$

where $\mathbf{F}_x(\mathbf{U})$ and $\mathbf{F}_r(\mathbf{U})$ represent the convective fluxes and $\mathbf{D}_x(\mathbf{U})$ and $\mathbf{D}_r(\mathbf{U})$, the diffusive fluxes. The origin of the two additional source terms $\mathbf{S}_e(\mathbf{U})$ and $\mathbf{S}_v(\mathbf{U})$ is purely geometric and stems from the choice of writing the system in a form that mimics as much as possible that obtained in a 2-D Cartesian co-ordinate system. If one denotes by $\theta$ the orthoradial direction, the components of the various fluxes are given by

$$\mathbf{F}_x(\mathbf{U})=\begin{pmatrix}\overline{\rho}\tilde{v}_x\\ \overline{\rho}\tilde{v}_x^2+\overline{p}\\ \overline{\rho}\tilde{v}_x\tilde{v}_r\\ \tilde{v}_x(\overline{\rho}\tilde{E}+\overline{p})\end{pmatrix},\quad \mathbf{F}_r(\mathbf{U})=\begin{pmatrix}\overline{\rho}\tilde{v}_r\\ \overline{\rho}\tilde{v}_x\tilde{v}_r\\ \overline{\rho}\tilde{v}_r^2+\overline{p}\\ \tilde{v}_r(\overline{\rho}\tilde{E}+\overline{p})\end{pmatrix} \tag{2}$$

$$\mathbf{D}_x(\mathbf{U})=\begin{pmatrix}0\\ \overline{\tau}_{xx}-\overline{\rho v_x'' v_x''}\\ \overline{\tau}_{xr}-\overline{\rho v_x'' v_r''}\\ \tilde{v}_x(\overline{\tau}_{xx}-\overline{\rho v_x'' v_x''})+\tilde{v}_r(\overline{\tau}_{xr}-\overline{\rho v_x'' v_r''})+\overline{\lambda\dfrac{\partial T}{\partial x}}-\overline{\rho v_x'' h''}\end{pmatrix}$$

$$\mathbf{D}_r(\mathbf{U})=\begin{pmatrix}0\\ \overline{\tau}_{xr}-\overline{\rho v_x'' v_r''}\\ \overline{\tau}_{rr}-\overline{\rho v_r'' v_r''}\\ \tilde{v}_x(\overline{\tau}_{xr}-\overline{\rho v_x'' v_r''})+\tilde{v}_r(\overline{\tau}_{rr}-\overline{\rho v_r'' v_r''})+\overline{\lambda\dfrac{\partial T}{\partial r}}-\overline{\rho v_r'' h''}\end{pmatrix} \tag{3}$$

$$\mathbf{S}_e=\frac{1}{r}\mathbf{F}_r(\mathbf{U})+\frac{1}{r}\begin{pmatrix}0\\ 0\\ \overline{p}+\overline{\tau}_{\theta\theta}+\overline{\rho v_\theta'' v_\theta''}\\ 0\end{pmatrix},\quad \mathbf{S}_v=\frac{1}{r}\mathbf{D}_r(\mathbf{U}) \tag{4}$$

In the above terms, $p$, $h$ and $\lambda$ stand for the static pressure, the enthalpy and the thermal conductivity, respectively. Assuming that the contribution of the fluctuations of velocity and temperature is



DOI: 10.1002/fld

negligible for the viscous and heat fluxes, the Reynolds average of the viscous tensor components and of the heat diffusion terms can be written as

$$\begin{cases} \overline{\tau}_{xx} \simeq \mu^* \left( \frac{4}{3} \frac{\partial \tilde{v}_x}{\partial x} - \frac{2}{3} \left( \frac{\partial \tilde{v}_r}{\partial r} + \frac{\tilde{v}_r}{r} \right) \right) \\ \overline{\tau}_{rr} \simeq \mu^* \left( \frac{4}{3} \frac{\partial \tilde{v}_r}{\partial r} - \frac{2}{3} \left( \frac{\partial \tilde{v}_x}{\partial x} + \frac{\tilde{v}_r}{r} \right) \right) \\ \overline{\tau}_{\theta\theta} \simeq \mu^* \left( \frac{4}{3} \frac{\tilde{v}_r}{r} - \frac{2}{3} \left( \frac{\partial \tilde{v}_x}{\partial x} + \frac{\partial \tilde{v}_r}{\partial r} \right) \right) \\ \overline{\tau}_{xr} \simeq \mu^* \left( \frac{\partial \tilde{v}_x}{\partial r} + \frac{\partial \tilde{v}_r}{\partial x} \right) \\ \overline{\lambda \frac{\partial T}{\partial x}} \simeq \frac{\mu^* \gamma C_v}{Pr} \frac{\partial \tilde{T}}{\partial x} \\ \overline{\lambda \frac{\partial T}{\partial r}} \simeq \frac{\mu^* \gamma C_v}{Pr} \frac{\partial \tilde{T}}{\partial r} \end{cases}$$

where the 'mean' molecular dynamic viscosity $\mu^*$ is expressed as a function of the mean temperature $\tilde{T}$ through a Sutherland's law formulation, $Pr$ is the Prandtl number, $\gamma$ is the specific heat capacity ratio and $C_v$ is the heat capacity at constant volume, supposed constant. The Reynolds stress tensor and the enthalpy turbulent fluxes are closed by a classical Boussinesq-like formulation for non-zero divergence flows, namely:

$$\begin{aligned} -\overline{\rho v_x'' v_x''} &= \mu_t \left( \frac{4}{3} \frac{\partial \tilde{v}_x}{\partial x} - \frac{2}{3} \left( \frac{\partial \tilde{v}_r}{\partial r} + \frac{\tilde{v}_r}{r} \right) \right) - \frac{2}{3} \overline{\rho} k, \quad -\overline{\rho v_x'' h''} = \frac{\mu^*}{Pr_t} \frac{\partial \tilde{h}}{\partial x} \\ -\overline{\rho v_r'' v_r''} &= \mu_t \left( \frac{4}{3} \frac{\partial \tilde{v}_r}{\partial r} - \frac{2}{3} \left( \frac{\partial \tilde{v}_x}{\partial x} + \frac{\tilde{v}_r}{r} \right) \right) - \frac{2}{3} \overline{\rho} k, \quad -\overline{\rho v_r'' h''} = \frac{\mu^*}{Pr_t} \frac{\partial \tilde{h}}{\partial r} \\ -\overline{\rho v_\theta'' v_\theta''} &= \mu_t \left( \frac{4}{3} \frac{\tilde{v}_r}{r} - \frac{2}{3} \left( \frac{\partial \tilde{v}_x}{\partial x} + \frac{\partial \tilde{v}_r}{\partial r} \right) \right) - \frac{2}{3} \overline{\rho} k \\ -\overline{\rho v_x'' v_r''} &= \mu_t \left( \frac{\partial \tilde{v}_x}{\partial r} + \frac{\partial \tilde{v}_r}{\partial x} \right) \end{aligned} \tag{5}$$

where $\mu_t$ is the eddy viscosity coefficient introduced by such a closure. This set of equations is supplemented by the equation of state which reads:

$$\overline{p} = (\gamma - 1) \overline{\rho} \left( \tilde{E} - \frac{\tilde{v}_i \tilde{v}_i}{2} - k \right) \tag{6}$$

where $k$ is the turbulent kinetic energy. The $k$–$\varepsilon$ turbulence model retained to express the coefficient of turbulent viscosity $\mu_t$ is presented in the following subsection.

### 2.2. Turbulence modeling

Assuming that Morkovin's hypothesis holds, the methodology applied to model incompressible turbulent flows [23] can be extended to deal with compressible turbulent flows. Accordingly, using



DOI: 10.1002/fld

the decomposition of the variables previously introduced, the transport equation for the turbulent kinetic energy $k$ is given by [24]

$$\frac{\partial(\overline{\rho}k)}{\partial t}+\frac{\partial(\overline{\rho}\tilde{v}_x k)}{\partial x}+\frac{1}{r}\frac{\partial(r\overline{\rho}\tilde{v}_r k)}{\partial r}=\frac{\partial}{\partial x}\left[\left(\mu^*+\frac{\mu_t}{\sigma_k}\right)\frac{\partial k}{\partial x}\right]+\frac{1}{r}\frac{\partial}{\partial r}\left[r\left(\mu^*+\frac{\mu_t}{\sigma_k}\right)\frac{\partial k}{\partial r}\right] + P_k+G+\Pi_d-\overline{\rho}\varepsilon \tag{7}$$

with $\sigma_k=1.0$. The production term $P_k$ is classically given by

$$P_k=-\overline{\rho v_x'' v_x''}\frac{\partial\tilde{v}_x}{\partial x}-\overline{\rho v_r'' v_r''}\frac{\partial\tilde{v}_r}{\partial r}-\overline{\rho v_\theta'' v_\theta''}\frac{\tilde{v}_r}{r}-\overline{\rho v_x'' v_r''}\left(\frac{\partial\tilde{v}_x}{\partial r}+\frac{\partial\tilde{v}_r}{\partial x}\right) \tag{8}$$

where the Reynolds-stress expressions are given in Equation (5). The term $G$ that represents the correlations between the velocity fluctuations and the mean pressure gradients, assimilated to an enthalpic production term, may induce an important negative contribution in regions of large density or pressure variations such as strong compression or expansion zones. Two closure expressions for this term will be tested, namely:

$$G=-\frac{1}{\rho}\frac{\nu_t}{\sigma_t}\left(\frac{\partial\overline{\rho}}{\partial x}\frac{\partial\overline{p}}{\partial x}+\frac{\partial\overline{\rho}}{\partial r}\frac{\partial\overline{p}}{\partial r}\right) \tag{9}$$

or

$$G=C_1\left(\frac{\gamma-1}{\gamma\overline{p}}\right)\left[\frac{\mu_t\gamma C_v}{Pr_t}\left(\frac{\partial\tilde{T}}{\partial x}\frac{\partial\overline{p}}{\partial x}+\frac{\partial\tilde{T}}{\partial r}\frac{\partial\overline{p}}{\partial r}\right)+\tilde{v}_x\frac{\partial\overline{p}}{\partial x}(-\overline{\rho v_x'' v_x''}-\overline{\rho v_x'' v_r''}) + \tilde{v}_r\frac{\partial\overline{p}}{\partial r}(-\overline{\rho v_x'' v_r''}-\overline{\rho v_r'' v_r''})\right] \tag{10}$$

The first closure expression of $G$ is quite commonly used even in situations involving dilatable flows such as in subsonic impinging flames simulations [25]. Following Bailly *et al.* [26], the coefficient $\sigma_t$, to be chosen in the interval [0.7–1], will be given the value $\sigma_t=0.7$. In deriving the second expression for $G$, Shyy and Krishnamurthy [24] supposed that the total enthalpy and the heat capacity remain constant and that the density fluctuations are isobaric. They expressed the parameter $C_1$ as a function of the turbulent Mach number $M_t$ by $C_1=2M_t/(1-M_t)$ with $M_t=\sqrt{2k}/a^*$, where $a^*$ is the 'mean' sound speed i.e. $a^*=\sqrt{\gamma r\tilde{T}}$. The pressure-dilatation term $\Pi_d$ is an additional work induced by simultaneous fluctuations of the pressure and the volume of the fluid particles. It can generally induce a considerable negative contribution to the balance of turbulent kinetic energy in the case of a shock/turbulence interaction. The two most popular approaches suggested in the literature will be considered. On the one hand, by combining the transport equations for the entropy and the density fluctuations, Zeman [27] suggested that this term can be linked to the pressure variance which is supposed to decrease toward an equilibrium value during a characteristic time which has to be evaluated. The consideration of a linear decrease of the



DOI: 10.1002/fld

pressure variance and the choice of the turbulent Mach number $M_t$ to represent this characteristic time lead thus to the following expression:

$$\Pi_d = \begin{cases} -C_d 2\overline{\rho}\dfrac{k^2}{\varepsilon} S_{ij}^* S_{ij}^*, & M_t \geqslant 0.1\sqrt{\dfrac{\gamma+1}{2}} \\ 0, & M_t < 0.1\sqrt{\dfrac{\gamma+1}{2}} \end{cases} \tag{11}$$

where $S_{ij}^*$ are the components of the deviatoric part of the deformation tensor. It should be noted that this model suffers from a large variability of the values adopted for the constant $C_d$. A value of 0.004 has been retained for our simulations according to previous tests performed for nearly transonic impacting jet configurations.[§] On the other hand, analysing results of direct numerical simulations for free homogeneous shear flows, Sarkar *et al.* [18] showed that only the incompressible part of the field of pressure can really modify the balance of turbulent kinetic energy. Using $M_t^2$ to represent the ratio of the compressible part of the turbulent kinetic energy to the total one, an asymptotic development, on an acoustic time scale, of the linear and the quadratic components of the incompressible field of the pressure through the Poisson equations of these, leads Sarkar *et al.* [18] to propose the following expression for the pressure-dilatation term in isotropic configurations:

$$\Pi_d = -0.4 P_k M_t^2 + 0.2\overline{\rho}\varepsilon_s M_t^2 \tag{12}$$

where the retained constants have the values initially recommended for plane shear layers and where $\varepsilon_s$ stands for the solenoïdal part of the turbulent kinetic energy dissipation rate. Finally, the last term of the right-hand side of Equation (7) that has to be calculated is the dissipation rate $\overline{\rho}\varepsilon = \overline{\rho}\varepsilon_s + \overline{\rho}\varepsilon_c$ considered as being the sum of the solenoïdal part $\varepsilon_s$ plus the dilatational part $\varepsilon_c$. The common practice followed here is to solve a transport equation for $\varepsilon_s$ while modeling $\varepsilon_c$. Accordingly, the transport equation of the solenoïdal dissipation rate is written as

$$\frac{\partial(\overline{\rho}\varepsilon_s)}{\partial t} + \frac{\partial(\overline{\rho}\tilde{v}_x\varepsilon_s)}{\partial x} + \frac{1}{r}\frac{\partial(r\overline{\rho}\tilde{v}_r\varepsilon_s)}{\partial r} = \frac{\partial}{\partial x}\left[\frac{\mu_t}{\sigma_\varepsilon}\frac{\partial\varepsilon_s}{\partial x}\right] + \frac{1}{r}\frac{\partial}{\partial r}\left[r\frac{\mu_t}{\sigma_\varepsilon}\frac{\partial\varepsilon_s}{\partial r}\right] + \frac{\varepsilon_s}{k}y[C_{\varepsilon_1}(P_k+G) - C_{\varepsilon_2}\overline{\rho}\varepsilon_s]$$

with $\sigma_\varepsilon = 1.0$. Two classical formulations are considered to express the dilatational dissipation rate $\varepsilon_c$. The first one, suggested by Zeman [28] and based on theoretical considerations about the additional dissipation induced by a given statistic distribution of 'shocklets' within the flow, reads as

$$\varepsilon_c = \begin{cases} 0.75\left(1 - \exp\left(-\left(\dfrac{M_t - M_{t0}}{\sigma_0}\right)^2\right)\right), & M_t \geqslant M_{t0} \\ 0, & M_t \leqslant M_{t0} \end{cases} \tag{13}$$

[§] According to the Simulog-Incka company which developed the CFD code N3S-NATUR, this constant value has been retained from various simulation tests of nearly transonic impacting jet configurations (Private communication, 2005).



DOI: 10.1002/fld

where $M_{t0}=0.1\sqrt{(\gamma+1)/2}$ and $\sigma_0=0.6$ are the values initially recommended for plane shear layers. On the other hand, by considering direct numerical simulation results and using asymptotic analysis, Sarkar *et al.* [18] suggest the following closure:

$$\varepsilon_c=\alpha_c M_t^2 \varepsilon_s \tag{14}$$

where $\alpha_c=0.5$ is the recommended value when the dilatational dissipation rate and the pressure-dilatational term are simultaneously taken into account. Finally, the closure of the system of governing equations is achieved once the coefficient of turbulent eddy viscosity is expressed as a function of $k$ and $\varepsilon$ by

$$\mu_t=C_\mu \overline{\rho}\frac{k^2}{\varepsilon} \tag{15}$$

In some simulations reported in the literature [26], $\mu_t$ is calculated by using the sole solenoidal dissipation rate $\varepsilon_s$. We should remark that this can lead to a significant difference with values obtained with Equation (16) when the Mach number increases. It is clear that the inclusion of $\varepsilon_c$ into the expression of $\mu_t$ reinforces the decrease of the turbulent diffusion by decreasing the level of the turbulent stress in the hydrodynamic transport equations as well as the production $P_k$ in the $k$ equation. In addition, expressing $\varepsilon_c$ as a function of $\varepsilon_s$ as it is done with the corrections of Sarkar *et al.* [18] or Zeman [27], and adding these two contributions to close $\mu_t$ is equivalent to considering only the solenoïdal dissipation with a modified value for $C_\mu$. As a consequence, taking only $\varepsilon_s$ into account to express $\mu_t$ may be seen as choosing a new constant $C_\mu$ more adapted to the particular flow geometry under study. Given that these dissipative corrections have been originally devised for plane shear layers and that the balance of turbulent kinetic energy is highly dominated by the production and dissipation terms, it seems natural, if not pragmatic, to check the relative influence of these two expressions of $\mu_t$ (with $\varepsilon$ or solely $\varepsilon_s$) in order to determine the most adapted level of turbulent diffusion to introduce.

### *2.3. Numerical method*

The numerical resolution of Equation (1) is based on the mixed finite-volume/finite-element method originally implemented in the CFD code N3S-NATUR [27], which is used and developed for this study. In order to approximate the weak form of the integral formulation of Equation (1), a cell-vertex approach on unstructured triangular meshes is used. The construction of each control volume is illustrated in Figure 2. The boundary $\Gamma_i$ of each surface $C_i$ is formed by linking the middles of the segments $M_{ij}$ between the node $i$ and each neighboring node $j$ with the centers of gravity $G_k$ of each neighboring triangle $T_k$ sharing this node $i$.

Firstly, the integration of the divergence of diffusive fluxes along $\Gamma_i$ is performed by using the finite element P1 on each triangle intersecting $C_i$. Secondly, a finite volume approximation is used to perform the integration of the convective terms. The numerical flux $F_{ij}$ along each interface $\Gamma_{ij}$ shared both by $\Gamma_i$ and $\Gamma_j$ is evaluated according to the mean direction $n_{ij}$ normal to $\Gamma_{ij}$ by applying either the flux splitting method of Van Leer [29] or the linearization of Roe [30] combined with the entropy fix of Harten [31]. To this end, the implemented hyperbolic solver relies on the total variation diminishing (TVD) procedure used to extrapolate the two adjacent constant mean values $U_{ij}=U_i+\frac{1}{2}(\nabla U)_{ij}.ij$ and $U_{ji}=U_j-\frac{1}{2}(\nabla U)_{ij}.ij$ on the left and on the right of $\Gamma_{ij}$, respectively. The gradient $(\nabla U)_{ij}$ is here selected by applying either a limiter function 'minmod' on the gradients of the physical variables encountered on the triangles intersecting the two adjacent



DOI: 10.1002/fld

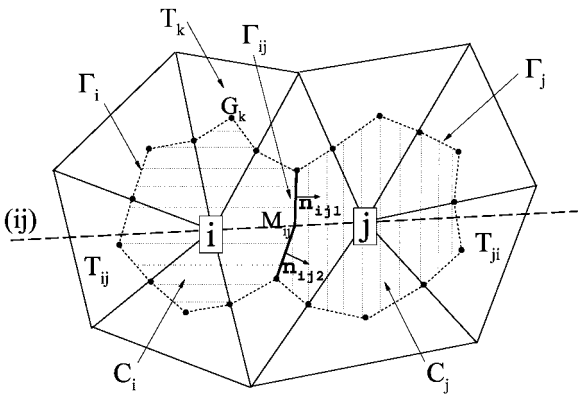


Figure 2. Schematic of the dual control volume associated with the mixed FV–FE method.

control volumes, or by applying a Van Albada limiter (defined by the function limiter $(a,b)=((a^2+\varepsilon)\cdot b+(b^2+\varepsilon)a)/(a^2+b^2+2\varepsilon)$, where $\varepsilon$ is a very small non-zero constant value) to a centered gradient $(\nabla U)_{ij}\cdot ij=V_j-V_i$ and a half-upwind gradient $(\nabla U)_{ij}\cdot ij=\frac{1}{2}(V_j-V_i+(\nabla_{T_{ij}}V)\cdot ij)$. In the latter case, the single gradient $(\nabla_{T_{ij}}V)$ is evaluated by the finite element on the upwind triangle intersecting the direction given by $(ij)$ (see Figure 2). Finally, in order to avoid a lack of robustness observed when some implicit temporal schemes are used to perform these simulations of highly underexpanded jets, an elementary Euler explicit scheme is retained for this first approach to perform the temporal integration. Within the framework of the Reynolds average Navier–Stokes simulation retained, the transitional behavior of the solutions is not considered as being meaningful, so that only the final converged solutions are observed and analyzed. Whatever the exact dependency of the path of convergence to the Courant–Friedrichs–Lewy (CFL) number retained, the final converged solution was found to be CFL independent. Accordingly, the CFL number is only chosen as the best compromise between the stability requirements and the computational time. A value of 0.8 has been found to be adequate for this study. The resulting time-step limitation is compensated by running the calculations in parallel on a MPI-Linux cluster, thanks to a domain decomposition algorithm.

## 3. SPECIFIC ISSUES RELATED TO HIGHLY UNDEREXPANDED JETS' SIMULATIONS

Whereas the numerical treatment previously presented is robust enough for most of the jet simulations generally performed, some particular difficulties are encountered in the case of highly underexpanded jets (with an NPR typically greater than 5). This section focuses on the reasons for these difficulties which motivate the choice of the particular methodology adopted and presented in the following part.

### *3.1. Robustness of the hyperbolic solver*

The coexistence of the first intense expansion zone and the strong shocks encountered in highly underexpanded jets leads to problems of lack of robustness and positivity of the upwind numerical schemes retained. On one hand, the 'minmod' limiter is known to be strongly dissipative [32] but



DOI: 10.1002/fld

any other limiter is not likely to be robust enough *a priori* when NPR is high. On the other hand, for moderate values of the NPR, Satyanarayana and Balkrishnan [33] have shown that using the Roe scheme with an adaptive mesh can lead to some solutions which nevertheless yield the same level of accuracy obtained with more sophisticated schemes such as the AFVS scheme ('Acoustic Flux Vector Splitting') or the KFVS scheme ('Kinetic Flux Vector Splitting'). In addition, in the framework of the retained way of building the control volumes, it should be noted that Roe's scheme can lead to very satisfying levels of robustness and accuracy on other classical benchmark configurations [34] such as the subsonic or supersonic Sod test case, the reflection of non-stationary shocks on a wedge or supersonic flows impacting on a blunt body or a forward facing step. In fact, in the case of highly underexpanded jet simulations, only this scheme can lead to a first correct solution. Whatever the initial grid topology and the initial grid density used, the solver of Van Leer or the use of the Van Albada limiter function leads to the failure of the calculations if they are used at the beginning of the simulation. Numerous investigations, beyond the scope of this study, on new variant of combination of numerical scheme and limiting functions would be required to highlight the exact behavior of these schemes in the particular framework of the mixed finite-volume/finite-element formulation retained. In fact, for initial simulations of highly underexpanded jets, Van Leer's scheme seems to suffer from an over-diffusion of the developing shear layer and the emerging slip line at the triple point, leading to an incorrect initial curvature of the Mach disk, which leads rapidly to bifurcate toward an unphysical solution. Then, the minmod limiter cancels for any node as soon as a change of the sign of the gradients is detected within the triangular cells surrounding and sharing this node. This gives an isotropic and very dissipative behavior to the resulting scheme. However, the Van Albada limiting function consists in using only a combination of an average value of the gradient calculated around each node and a second estimation found within a single other triangle chosen according to the specific direction given by the segments connecting this node to its neighboring nodes. Thus, as long as the mesh is not stretched along the strong discontinuities, a change of the sign of the gradients in the tangential direction to the discontinuities may not be strictly detected and the use of the Van Albada limiting function might result in a lack of stabilizing numerical diffusion in those directions during the initial phase of the calculation. Accordingly, in a first approach, Roe's method combined with the minmod limiter and the entropy fix of Harten is retained for the robustness and the simplicity of the resulting numerical scheme.

### *3.2. Grid topology and refinement*

Upwind procedures are generally developed for one-dimensional flows before being applied for multidimensional flows by choosing a direction of evaluation. Most of the time, the flux equilibrium for each control volume is thus updated by precisely evaluating the projection of the mean convective flux on the mean direction normal to its interfaces instead of evaluating the mean convective flux itself. When strong shocks are simulated, any privileged mean direction given by $n_{ij}$ (if the grid is based, for example, on regularly split structured meshes) leads to a dramatic propagation of numerical instabilities and often to non-physical solutions. The numerical artifact observed is very similar, in this case, to the famous carbuncle phenomenon from a geometric point of view but could not be avoided by additional numerical dissipation. Thus, the only way to compensate the propagation of this numerical error is to use irregular meshes of Voronoï type for the initial grid. Nevertheless, for quite similar reasons, the very strong diffraction shock encountered in the initial phase of the simulation can lead to a failure of the calculations if this initial grid is too



DOI: 10.1002/fld

refined, even if this mesh is of Voronoï type. On the contrary, it should be stressed that too coarse an initial grid cannot be used because it would also lead to a non-physical solution. Typically, an overly dissipated barrel shock leads to a Mach disk yielding an inverted curvature followed by a non-physical recirculation and so inhibits any relevant application of a re-adaptation procedure. Accordingly, a compromise has to be found at first for the initial density of the grid which has to be of Voronoï type and the choice of an adaptive meshing procedure might be guided then in order to help realign at best the mean directions used to evaluate the convective flux on each control volume with the directions of propagation of the characteristics information.

### *3.3. Field variables initialization and boundary conditions*

The simulation cases considered for this study mainly correspond to jet experiments performed with converging nozzles designed to give top-hat profiles of the physical variables at the nozzle exit. With a view to limiting as far as possible the cost of the simulations, the exact nozzle geometry and the boundary layers are so neglected for this preliminary study and the simulations are only performed downstream of the orifice section. Thus, the real geometry of the nozzle lip is simplified and only slip wall conditions are prescribed through the flux components. The Mach number at this nozzle inlet boundary is imposed to 1.01 in order to ensure the robustness of the simulations. Accordingly, the values of the physical variables corresponding to an isothermal underexpanded jet yielding the desired NPR are prescribed in the flux components through the segments belonging to this nozzle inlet section.

Similarly, for simulations robustness enhancement objective, a very slow coflow at a Mach number of 0.05 is imposed at the boundary located upstream of the nozzle inlet section as shown in Figure 3 (segment F12).

Even if a slight coflow is added, the static pressure calculated at some points near the orifice edge can become slightly too high due to the non-realistic presence of a singular point at the edge of the nozzle wall. This results in a slight shift of the overall shock structure downstream of its expected location. Such a numerical artifact has been remedied by introducing a pseudo-nozzle lip corresponding to the two additional boundary segments F6 and F7 as shown in Figure 3.

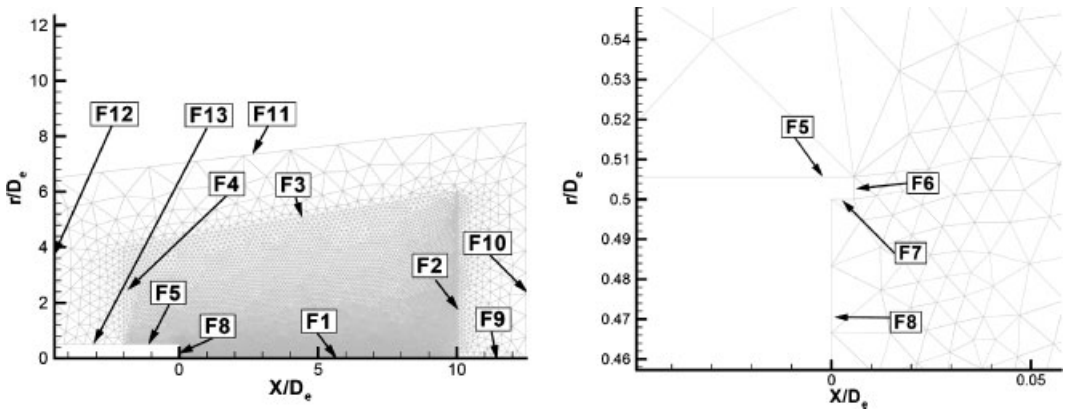


Figure 3. Overview of the computational domain (left) and zoom at the inlet boundary featuring the pseudo-nozzle lip (right).



DOI: 10.1002/fld

The length of these segments is equal to 0.005 times the orifice diameter. The introduction of this simple and small pseudo-nozzle lip does not modify the geometric features of the expected jet structure and prevents too great a shift of the levels of the physical variables calculated at the wall.

The nodal values of the computational domain are usually initialized with the physical state corresponding to the coflow characteristics. But, in such a case, during the initial phase of the calculation, a low-density recirculation zone, which appears at the jet boundary, is convected downstream and is partially reflected at the outlet boundary. In order to limit the strength of such a vortex, the nodal values are initialized with a physical state chosen to correspond to a Mach number value of 0.5. Combined with the use of the buffer zone described below, this artificial low-density region can thus be rapidly evacuated from the computational domain.

Focusing now on the outlet boundary, the application of the one-dimensional theory of characteristics leads to consider that only one physical information (the pressure) has to be prescribed at the boundary segments if the outgoing flow is subsonic. On short computational domains, such a pressure profile is quite difficult to determine since the pressure prevailing in the subsonic coflow does not match the pressure downstream of the Mach disk. It is all the less obvious to adapt these levels of static pressure as a function of a theoretical for constant level of total pressure since the decrease in the total pressure is more important through the Mach disk than through the oblique reflected shock. In order to prescribe a more correct level of pressure in this zone near the axis for confined underexpanded jets, Prudhomme and Haj-Hariri [21] have suggested extrapolating the pressure found at the nearest point found within the shear layer where a supersonic state is detected. However, after some initial tests, this methodology has not been retained here since it proved to be insufficient to avoid the appearance of artificial recirculation zones upstream of the outlet section when large values of NPR were considered. Indeed, for such high-speed jets, the air entrainment from the coflow is sufficiently high to significantly modify the static pressure profile at the subsonic jet boundary. As a consequence, the prescription of two not perfectly appropriate different constant profiles of static pressure or total pressure at the subsonic outlet boundaries of the computational domain induces artificial total pressure differences upstream of these outlet boundaries and makes the shear layer bend slightly toward the axis. If the grid is refined enough in this zone, artificial numerical waves could then travel through the subsonic zone and destabilize the upstream structure. Considering that an appropriate profile of pressure (extrapolated from experimental data which are not available) cannot be prescribed at the exit, it appears necessary to dampen these artificial numerical waves as far as possible. Adding artificial viscosity upstream of the outlet boundary is not natural considering the upwind method applied throughout the computational domain. However, coarsening the grid in a specified zone upstream of this boundary is a way to reintroduce more naturally some local numerical diffusion. In return, this is in contradiction with the requirement to use grid adaptation within the near field to improve the spatial accuracy. In order to find a trade-off between these two opposite requirements (appropriate grid adaptation in the near field and strong coarsening upstream of the outlet boundary), a procedure of embedding of the core region within a larger zone, for which a coarsened mesh is employed, has been elaborated and is described in the next section. Since this procedure removes the requirement to prescribe accurate boundary conditions at the inlet or outlet section of the computational domain, a simple update of the physical variables has been used at these boundaries, based on the one-dimensional theory of characteristics according to the direction normal to the boundary segments. First, the number of incoming characteristics is evaluated from the local Mach number, in order to update the corresponding number of physical variables in ghost cells (subscripted by $g$) located beyond



DOI: 10.1002/fld

the boundaries. Based on far conditions corresponding to the quiescent atmosphere (subscripted by $\infty$), the level of the physical variables is updated by using the compatibility relations, that is,

$$\frac{p_g}{\rho_\infty^\gamma}=\frac{p_\infty}{\rho_\infty^\gamma},\quad u_g+\frac{2a_g}{\gamma-1}=u_\infty+\frac{2a_\infty}{\gamma-1}\quad\text{and}\quad u_g-\frac{2a_g}{\gamma-1}=u_\infty-\frac{2a_\infty}{\gamma-1}$$

respectively for the characteristics:

$$\frac{\mathrm{d}n}{\mathrm{d}t}=u_n,\quad \frac{\mathrm{d}n}{\mathrm{d}t}=u_n+a\quad\text{and}\quad \frac{\mathrm{d}n}{\mathrm{d}t}=u_n-a$$

These ghost cell values are then used directly to evaluate the convective flux components, according to the upwind numerical scheme used, while the viscous fluxes are neglected at these boundaries.

Last but not least, because of the initial flow field initialization retained, it should be highlighted that the initial expansion of the jet is nevertheless very important so that the flow direction and its physical state (subsonic or supersonic) cannot be strictly imposed at the boundary non-orthogonal to the axis represented by the segment F11 in Figure 3. Accordingly, the flux components at these boundaries are evaluated by an extension of the Steger–Warming scheme, namely:

$F(U_\mathrm{b},U_\infty)=\overline{\overline{A}}^{+}(U_\mathrm{b})U_\mathrm{b}+\overline{\overline{A}}^{-}(U_\mathrm{b})U_\infty$ where $U_\mathrm{b}$ is the conservative state vector found near the boundary, and $\overline{\overline{A}}=\overline{\overline{A}}^{+}+\overline{\overline{A}}^{-}$ is the jacobian matrix of the convective flux split into two parts according to the sign of its eigenvalues.

## 4. MESH ADAPTATION STRATEGY AND VALIDATION

### *4.1. Presentation of the overall procedure*

The overall strategy adopted to overcome the numerical difficulties previously described is illustrated in Figure 4. After the choice of an appropriate initial core grid and appropriate initial conditions (step 1), it mainly consists in building a thin but strongly coarsened zone around the core grid and merging these (step 2) before performing the first simulation (step 3). The converged solution obtained at this step within the buffer zone is highly diffused on purpose and so is not considered. Thus, the solution corresponding to the core domain is extracted (step 4) and used to apply the chosen adaptive meshing procedure and generate a new adapted core grid (step 5). Generating a new corresponding buffer zone and initializing the new overall grid based on the solution previously obtained, this overall cycle is repeated several times until a core grid convergence is reached. Depending on the level of NPR considered, two or three cycles are necessary. For each flow simulation (i.e. step 3), the criterion of convergence used is based on the L2 norm of the density (non-dimensionalized by its initial value) and is adapted for each level of NPR.

### *4.2. Grid adaptation algorithm*

The anisotropic mesh adaptation (AMA) algorithm of Dolejši [35] is chosen to progressively build the best adapted mesh for the core part of the grid. When an isotropic distribution of nodes is used in a finite triangular and linear element approach, the principle of the adaptation is based on the fact that the higher the curvature, the more important the interpolation error will be. Consequently, for a given level of grid density, the interpolation error can be decreased and more uniformly redistributed if the triangles are anisotropic and stretched normal to the isolines of the greatest



DOI: 10.1002/fld

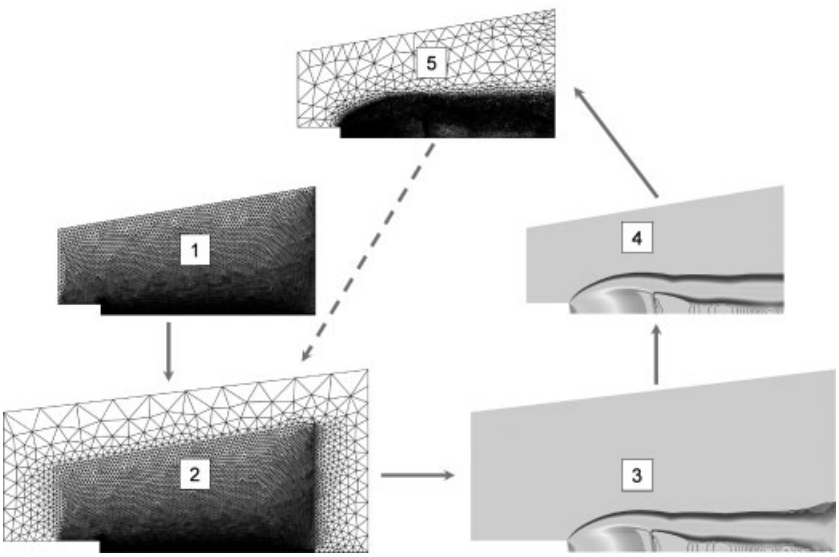


Figure 4. Illustration of the initial stages of the cycle of the mesh adaptation strategy adopted: step 1, initial core region mesh; step 2, embedding of the core mesh; step 3, flow simulation until convergence; step 4, extraction of the solution in the core region; step 5, remeshing of the core region and comparison with the previous core region mesh of step 1 to determine if a new cycle must be completed.

values of curvature. Thus, the method consists in evaluating the local curvature of a significant physical variable (the density for the present simulations of underexpanded jets) in order to build a new metric for which the ideal lengths of all triangle edges should be equal. In order to best set the lengths of the segments (locally evaluated with the new metric) to their ideal length, local operations of edge splitting, node removal or sweeping are thus iteratively applied. This method results not only in clustering nodes where the gradients are high and in reducing the number of nodes elsewhere but also in progressively lining up the triangular meshes with the various discontinuities. As a consequence, the accuracy of the evaluation of the convective fluxes is highly improved (within the limits of the relative one-dimensional upwind method).

### *4.3. Initial grid*

An iterative loop splitting algorithm [36] implemented in the 'QUAD' module of the mesh generator ICEMCFD has been chosen for generating the initial meshes. This algorithm has been retained in particular for its robustness and for the resulting mesh quality. The first loop considered is the polygonal closed line formed by linking each boundary segment of the core zone (segments F1–F8 in Figure 3). The imposition of a given mesh size at each of these segments leads to the initial distribution of nodes on the initial loop. Each loop is then iteratively split into two sub-loops by linking two nodes of the previous loop. The splitting segment is chosen based on an estimated error criteria used to lead to triangles as close as possible to equilateral triangles and to the shortest lengths of the splitting segments. On comparison with frontal methods, this initial meshing procedure generates fewer triangular elements near the boundaries where a very small mesh size is used (such as the pseudonozzle lip) while the transition of the mesh sizes throughout



DOI: 10.1002/fld

the computational domain is particularly regular. This latter advantageous characteristic is fully used to separately build a regularly coarsened buffer mesh on the surrounding domain (segments F4, F3, F2, F9–F13 in Figure 3).

### *4.4. Validation of the strategy adopted*

Two computational domains are considered for the validation of the strategy developed: a short domain with a length of $13.5D_e$ (core zone length $=10D_e$) and $30D_e$ long one (with a core zone length of $20D_e$). The effect of using a short computational domain surrounded by a coarsened grid proves to be marginal on the solutions of the near field as it is illustrated in Figure 5 for an inviscid jet at NPR $=7.55$.

Whatever the NPR considered (ranging from 1 to 15.53), converged solutions at each cycle are obtained with the present mesh adaptation strategy. For all turbulent jets' calculations, three cycles are enough to obtain a final core mesh and a corresponding flow solution which do not present further significant changes if additional cycles are performed. Figure 6 illustrates, for an underexpanded turbulent jet at NPR $=7.55$, the kind of mean longitudinal velocity component profile evolution observed during the course of the mesh adaptation cycles and the fairly global grid density independence which is obtained. The required grid density mainly depends on the extension of the discontinuities and thus on the value of NPR. For instance, for a highly underexpanded turbulent jet at NPR $=7.55$ and for the shortest computational domain, a 10 000-node mesh proved to yield satisfactory results after only three loops of mesh adaptation.

A zoom of the generated grid in the vicinity of the triple point, presented in Figure 7, illustrates how the mesh elements are suitably stretched and aligned along the various strong waves of discontinuities. The near-field solutions (say for $X/D_e<10$) obtained on the two computational domains are similar. The main difference between the two solutions is mainly restricted to the zone located near the axis just downstream of the Mach disk so that it appears to be related to a different distribution of nodes in the near zone but not to the presence of the buffer zone. As a consequence, the utilization of such a buffer zone enables not only a lessening of the reflexivity of the outlet boundary but also the natural imposition of a necessary piece of information within the subsonic zone downstream of the Mach disk.

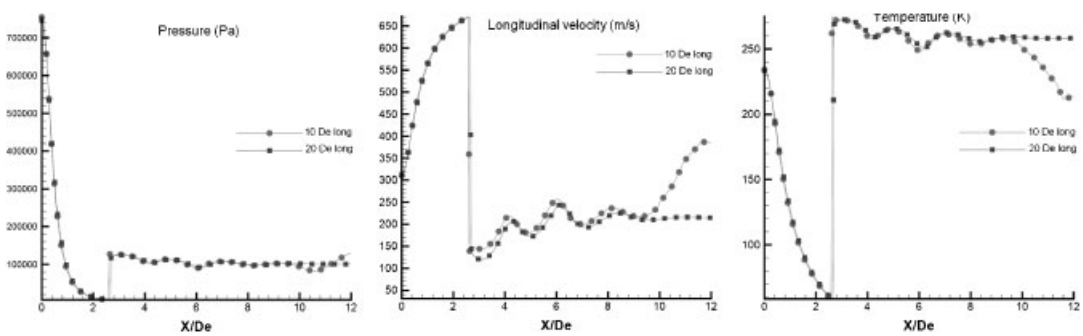


Figure 5. Influence of the length of the computational domain: comparison of the axial evolutions of the pressure, the longitudinal velocity and the temperature obtained on each computational domain ($10D_e$ and $20D_e$ long, respectively) for an inviscid jet at NPR $=7.55$.



DOI: 10.1002/fld

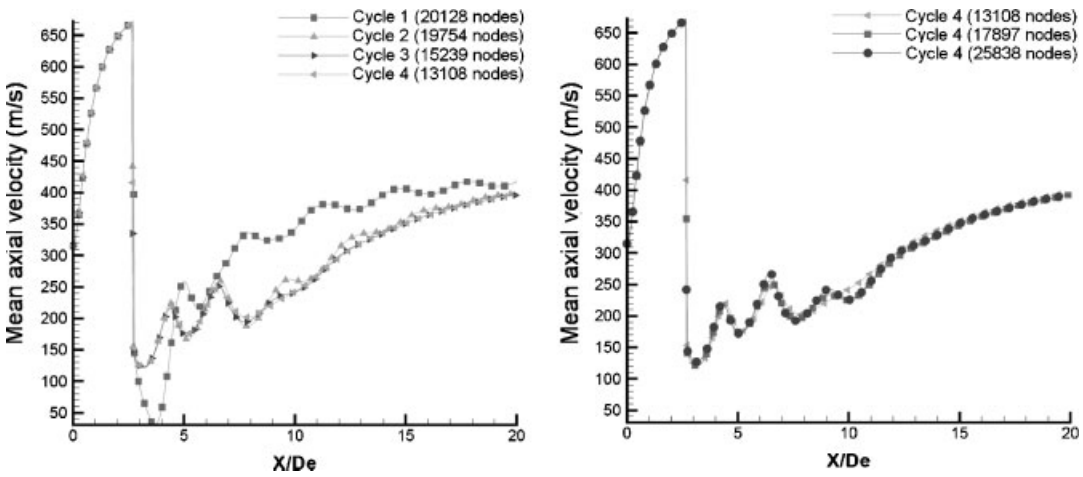


Figure 6. Sensitivity of the turbulent jet solution at NPR = 7.55 to the number of mesh adaptation loops (left) and to the prescribed number of grid nodes (right).

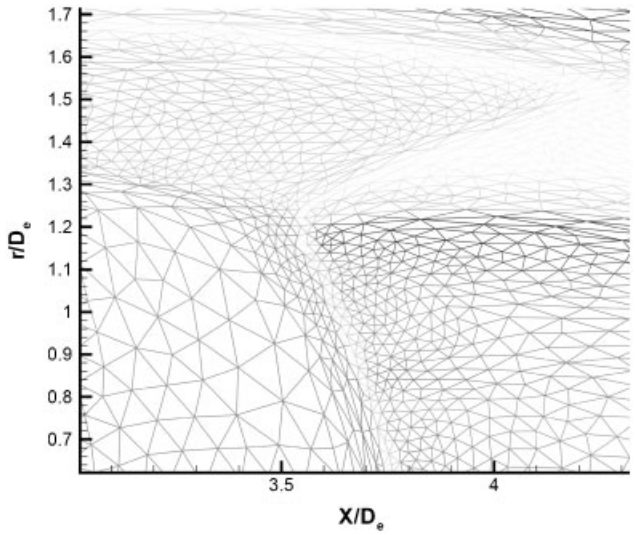


Figure 7. Illustration of the grid topology obtained around the triple point after three grid adaptation cycles for the simulation of an underexpanded turbulent jet at NPR = 15.53.

## 5. PERFECTLY EXPANDED JET SIMULATIONS

Most of the various approaches previously presented and retained to take the compressibility effects into account have already been directly and separately used for simulating axisymmetric underexpanded jets [17, 19]. Nevertheless, it should be recalled that these corrections have been initially adapted for two-dimensional shear layers. Thus, as a first evaluation step, these corrections



DOI: 10.1002/fld

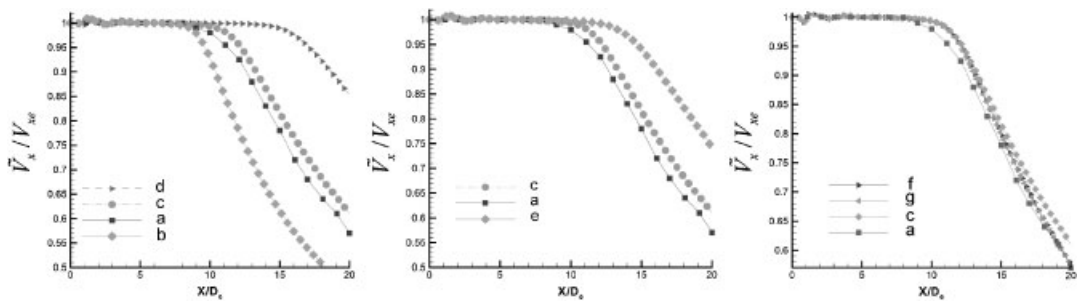


Figure 8. Perfectly expanded turbulent jet: evolutions of the mean longitudinal velocity component predicted by using various combinations of turbulence models corrections. a, experimental results of Seiner *et al.* [37]; b, standard $k$–$\varepsilon$ model; c, (respectively d) $k$–$\varepsilon$ model with addition of the pressure-dilatation and dilatational dissipation from Sarkar *et al.* [18] (respectively Zeman [27]) and with expressing $\mu t$ from the solenoidal dissipation; e, $k$–$\varepsilon$ model with addition of the pressure-dilatation and dilatational dissipation from Sarkar *et al.* [18] with expressing $\mu t$ from the total dissipation; f, (respectively g) $k$–$\varepsilon$ model with addition of the pressure-dilatation and dilatational dissipation from Sarkar *et al.* [18], the enthalpic production term from the gradient-type approximation (respectively Shyy and Krishnamurthy [24]) and by expressing $\mu t$ from the solenoidal dissipation.

have been tested on the configuration of a perfectly expanded axisymmetric jet experimentally studied by Seiner *et al.* [37]. In order to check also that the mesh re-adaptation procedure is fully valid for an axisymmetric jet configuration and to choose *a priori* the most appropriate combination of models for the various compressible terms presented in subsection 2.2, several perfectly expanded jet simulations are performed. The value of the exit Mach number is equal to 2 and is only slightly lower than the levels encountered within the shear layers considered for the higher levels of under-expansion tested and presented in the following section. This preliminary validation study is performed by prescribing a turbulence intensity corresponding to an amplitude of the longitudinal fluctuations equal to 5% of the mean velocity at the nozzle section, a length scale equal to $0.14D_e$ and the commonly adopted value of 0.7 for the turbulent Prandtl number. Roe's scheme is used and is combined with a minmod limiter and an entropy fix coefficient equal to 0.05, while the CFL number is set equal to 0.8. The initial core computational domain is $20D_e$ long and contains 20 128 nodes. Several possible combinations of models have been tested after a thorough check of the independence of the results to the initial grid density (with typically 6500 nodes in the core region for the adapted final mesh). Figure 8 presents a few examples of the predicted axial evolutions of the mean longitudinal velocity component (normalized by the mean velocity at the nozzle section $Vx_e$) corresponding to the solutions obtained with the different turbulence model combinations. One recovers the well-known tendency of the standard $k$–$\varepsilon$ model to introduce an excess of diffusion whereas the Zeman model yields an overly pronounced decrease of turbulent kinetic energy that can be mainly attributed to a lack of universality of the current constant retained for this model. Clearly, a full parametric study (beyond the scope of the present study) would be necessary to check whether this model could be easily improved for the present axisymmetric jet configuration. The contribution of the enthalpic production term $G$ appears to be quite marginal for this perfectly expanded jet with no noticeable difference related to the two expressions tested. Indeed, a marginal decrease of about 2% of the dimensionless velocity in the inertial zone at a distance from the orifice greater than about $15D_e$ can be typically observed when



DOI: 10.1002/fld

$G$ is taken into account. Nevertheless, the model of Shyy and Krisnamurthy will not be retained for jet simulations at higher NPRs, because its use leads quite systematically to a failure of the calculations when it is applied to highly underexpanded jet configurations, probably due to an excessive contribution of the shear stress components during the initial phase of the simulation.

Among the various model combinations tested, the best physical representation of the jet combined with a satisfactory level of robustness is obtained by using (i) a gradient-type closure for the enthalpic production; (ii) an expression of the turbulent viscosity coefficient based on the solenoïdal dissipation rate only; and (iii) the models of Sarkar *et al.* [18] for both the dilatational dissipation rate and the pressure-dilatation term. Accordingly, such a combination of model corrections, called the reference model in the following, will be adopted for the simulations of highly underexpanded jets. It is therefore given by

$$\begin{cases} \dfrac{\partial(\overline{\rho}k)}{\partial t}+\dfrac{\partial(\overline{\rho}\tilde{v}_x k)}{\partial x}+\dfrac{1}{r}\dfrac{\partial(\overline{\rho}r\tilde{v}_r k)}{\partial r} = \left(\mu+\dfrac{\mu_t}{\sigma_k}\right)\left(\dfrac{\partial^2 k}{\partial x^2}+\dfrac{\partial^2 k}{\partial r^2}+\dfrac{1}{r}\dfrac{\partial k}{\partial r}\right) \\ \qquad\qquad +(1-0.4M_t^2)P_k+G+-\overline{\rho}(1+0.3M_t^2)\varepsilon_s \\ \dfrac{\partial(\overline{\rho}\varepsilon_s)}{\partial t}+\dfrac{\partial(\overline{\rho}\tilde{v}_x \varepsilon_s)}{\partial x}+\dfrac{1}{r}\dfrac{\partial(\overline{\rho}r\tilde{v}_r \varepsilon_s)}{\partial r} = \left(\mu+\dfrac{\mu_t}{\sigma_\varepsilon}\right)\left(\dfrac{\partial^2 \varepsilon_s}{\partial x^2}+\dfrac{\partial^2 \varepsilon_s}{\partial r^2}+\dfrac{1}{r}\dfrac{\partial \varepsilon_s}{\partial r}\right) \\ \qquad\qquad +\dfrac{\varepsilon_s}{k}(C_{\varepsilon 1}(P_k+G)-C_{\varepsilon 2}\overline{\rho}\varepsilon_s) \end{cases} \tag{16}$$

with

$$\begin{aligned} P_k &= -\overline{\rho v_r'' v_r''}\frac{\partial \tilde{v}_r}{\partial r}-\overline{\rho v_r'' v_r''}\frac{\partial \tilde{v}_r}{\partial r}-\overline{\rho v_\theta'' v_\theta''}\frac{\tilde{v}_r}{r}-\overline{\rho v_x'' v_r''}\left(\frac{\partial \tilde{v}_x}{\partial r}+\frac{\partial \tilde{v}_r}{\partial x}\right) \\ G &= -\frac{1}{\overline{\rho}}\frac{\upsilon_t}{\sigma_t}\left(\frac{\partial \overline{\rho}}{\partial x}\frac{\partial \overline{p}}{\partial x}+\frac{\partial \overline{\rho}}{\partial r}\frac{\partial \overline{p}}{\partial r}\right) \\ \mu_t &= C_\mu \overline{\rho}\frac{k^2}{\varepsilon_s} \end{aligned} \tag{17}$$

By using this reference model, the jet growth characteristics and the self-similar behavior in the near zone are correctly reproduced as it is illustrated in Figure 9 where $r(0.5)$ is the location at which half of the axial velocity $V$-axis is found and $\delta c = r(0.95)-r(0.05)$ is the width of the shear layer estimated from the locations where the values corresponding to 5 and 95% of the axial velocity are reached. The fact that the initial spreading of the jet is underestimated could be related to an overestimation of the entrainment of the coflow at the jet boundary near the exit when compared with what is experimentally observed.

## 6. HIGHLY UNDEREXPANDED JET SIMULATION RESULTS

Two jet configurations experimentally studied by Yüceïl *et al.* [38, 39] have been simulated. They correspond to NPR = 7.55 and 15.53, respectively.



DOI: 10.1002/fld

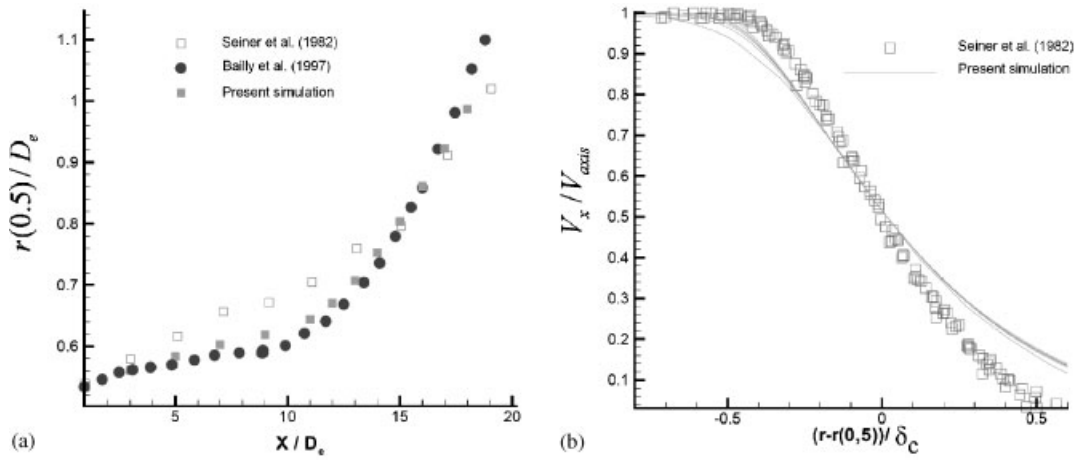


Figure 9. Perfectly expanded jet—simulations with the reference turbulence model: (a) evolution of the distance where half of the axial velocity is reached and (b) self-similar behavior of the profiles of the mean longitudinal velocity component for $X/D_e = 1$, 3, 5, 7, 9 and 11 (solid lines).

### 6.1. *Sensitivity to the numerical solver*

Because of a lack of robustness during the initial phase of the calculation, the Van Leer/Van Albada limiter could not be used for NPR greater than 1, whereas Van Leer's flux splitting method coupled with the use of a minmod limiter could be used only from the second cycle of the simulation. Nevertheless, switching from Roe's solver to Van Leer's solver from this second cycle results in quite the same final jet structure and as a consequence, Roe's algorithm is preferred for its robustness and is used to obtain the solutions presented in the following subsections.

### 6.2. *Representation of the near jet structure*

A qualitatively correct representation of the jet structure is predicted as it can be seen in Figure 10. The adaptation of the static pressure is mainly realized through the near shock structure as it is supposed to be from a theoretical point of view. Owing to the important difference of total pressure found between each side of the slip line, three couples of expansion and compression zones are visible within the supersonic layer and the overall adaptation mechanism is carried on up to a distance of about $10D_e$ from the nozzle section, which is in agreement with the experimental observations of Yüceïl *et al.* [38, 39]. The accuracy of the geometric extension of the simulated shock structure at NPR = 15.53 is evaluated by comparing (i) the predicted value of the Mach disk location $X_{\mathrm{dm}}$ against the experimental data of Love [10], the value obtained from processing Schlieren visualizations provided by Yüceïl and Ötügen,[¶] the correlations of Ashkenas and Sherman [6] and Ewan and Moodie [7] and (ii) the predicted value of the Mach disk diameter $D_{\mathrm{dm}}$ with the value given by the correlation of Antsupov [8]. The different correlations are

[¶]Private communication, 2003.



DOI: 10.1002/fld

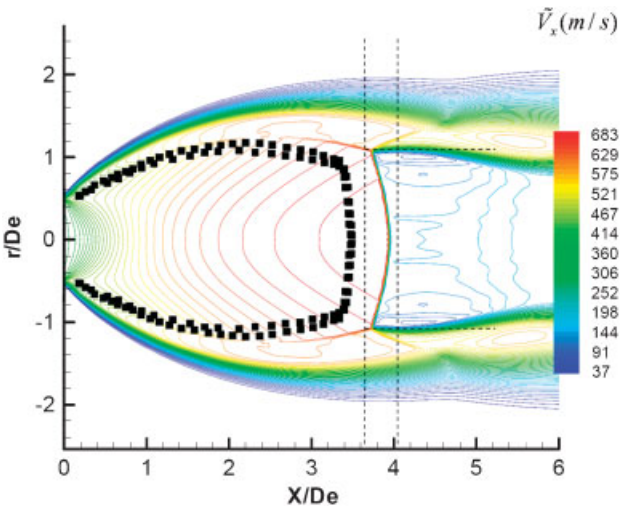


Figure 10. Underexpanded turbulent jet at NPR = 15.53—visualization of the near-jet structure: isolines of the mean longitudinal velocity component from the present simulations (solid lines) against (i) the experimental location of the shock structure from Yüceïl and Ötügen (symbols) and (ii) the domain of location given by the correlations of Equation (18) (dashed line).

given by

$$\frac{X_{\mathrm{dm}}}{D_e} = 0.67\sqrt{\frac{p_o}{p_a}}$$

$$X_{\mathrm{dm}} = 0.77D_e + 0.068D_e^{1.35}\left(\frac{p_e}{p_a}\right) \tag{18}$$

$$\frac{D_{\mathrm{dm}}}{D_e} = \log\left(\left(\frac{p_e}{p_a}\right)^{5/2}\right) - \frac{3}{4}$$

where $p_o$, $p_e$ and $p_a$ are the upstream total pressure, the static pressure at the inlet section and the static pressure of the ambient atmosphere, respectively. $D_e$ must be expressed in millimetres for the second following correlation yielding $X_{\mathrm{dm}}$.

The longitudinal extension of the first shock cell appears to be overestimated in the simulations and the simulated Mach disk yields a more important level of curvature than expected but with a quite correct radial extension. The most important discrepancy in the shock location is observed for the largest value of NPR tested and is estimated to be equal to 14% in terms of $X/D_e$.

In fact, this shift appears more clearly from a position located near the one where the barrel shock has reached its maximal extension and seems to be related to a failure of Roe's scheme when a limit value of the Mach number is reached during the expansion process. This hypothesis is confirmed by the comparisons of axial evolutions of velocity shown in Figure 11 for turbulent jet simulations at NPR = 7.55. The axial velocity appears to be overestimated not only in the expansion zone (up to +20%) but it also keeps on decreasing downstream of the Mach disk instead of increasing again by expansion of the surrounding supersonic layer. It thus seems to be



DOI: 10.1002/fld

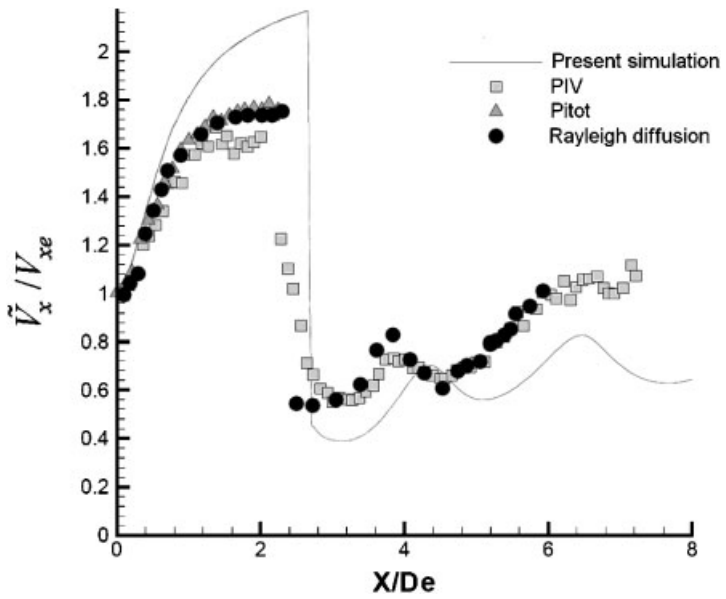


Figure 11. Underexpanded turbulent jet at NPR = 7.55: evolutions of mean longitudinal velocity component obtained from the present simulations and from the experimental results of Yüceïl *et al.* [38, 39].

only related to a perfectible shock geometry obtained around the triple point which leads to an initial slip line diverging toward the jet boundary instead of bending directly toward the axis. This suggests that the origin of such a numerical artifact could be related to the inaccurate straight profile of physical variables prescribed at the inlet boundary (Segment F8 in Figure 4), and so a separate study has been carried out to check the qualitative influence of the deformation of the profiles at this inlet section. The results obtained (by using isotropic mesh refinement within the near field) prove that the Mach disk diameter depends strongly on the initial inclination of the streamlines but that the same inaccurate levels of the Mach disk curvature are always observed whatever the profile prescribed at the inlet boundary and the method of mesh refinement used. As a consequence, this drawback may be mainly attributed to a weakness of the hyperbolic solver. Additional tests are required to find a more accurate but equally robust scheme than Roe's scheme.

### *6.3. Representation of the turbulent mixing*

In spite of the discrepancies observed for the velocity field within the potential core, the main features of the overall turbulent structure are correctly captured.

Figure 12 illustrates, for example, the typical development of the main shear layer surrounding the internal shear layer issued from the triple point at NPR = 7.55. The locations of the maximum shear stress are in good agreement with those extracted from the results of Yüceïl and Ötügen [38]. Whereas the levels of vorticity are largely overestimated at the jet boundary near the nozzle (twice as much i.e. $6E5\,s^{-1}$ instead of about $3E5\,s^{-1}$), these levels decrease rapidly downstream of the location where the shock extension is maximal to reach values of 1E5 to $1.5E5\,s^{-1}$ which are close to the experimental values. In addition, the observed overall development of these two uncoupled



DOI: 10.1002/fld

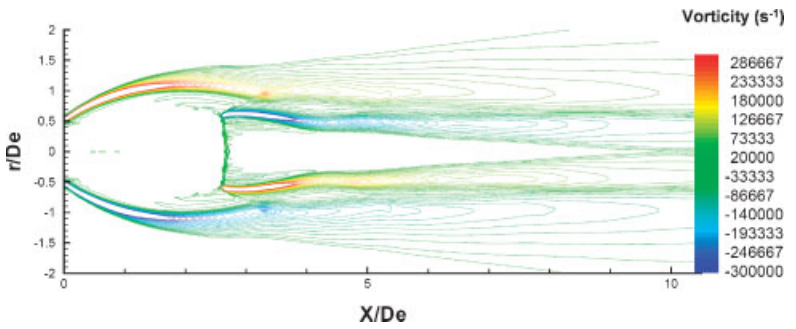


Figure 12. Underexpanded turbulent jet at NPR = 7.55: simulated mean vorticity field.

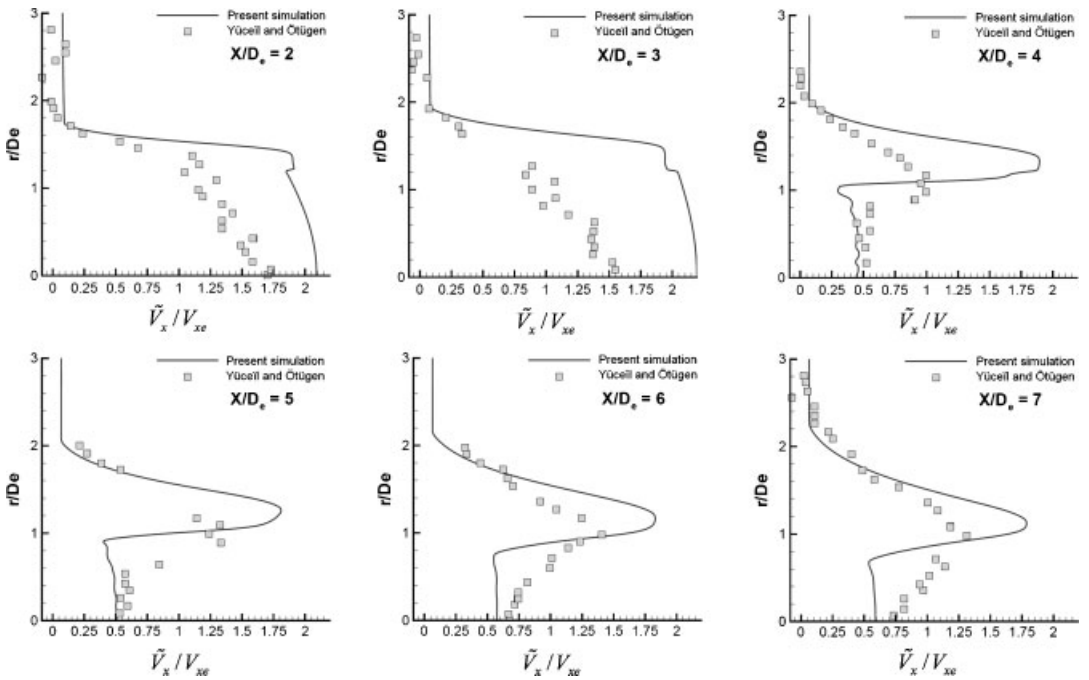


Figure 13. Underexpanded turbulent jet at NPR = 15.53: longitudinal evolution of the radial profiles of the mean longitudinal velocity component.

shear layers up to a distance of at least $7D_e$ is also in good agreement with the experimental observations. Nevertheless, by comparing the radial profiles of longitudinal velocity downstream of the Mach disk with the available experimental data at NPR = 15.53 (see Figure 13), it can be noted that the radial turbulent diffusion is underestimated. The predicted length of the potential core is equal to about $9D_e$, whereas the experimental profiles show that the shear layer reaches the axis for $X/D_e$ around 5 or 6. According to the validation of the chosen compressibility corrections previously presented for a perfectly expanded jet, these new results prove that the reference model



DOI: 10.1002/fld

remains incomplete when only compressibility corrections are added. Sarkar's correction only acts to decrease the level of $k$ within the shear layer (by 7 to about 20% from $X/D_e = 1$–5 for instance in the case of the perfectly expanded jet previously studied) without greatly modifying the dissipation rate. Besides, the effect of the enthalpic production remains marginal even for such high levels of baroclinic torque found within the near field. This results in a decrease of the global mixing in each of the shear layers, whereas the turbulent mixing is in fact highly increased downstream of the Mach disk of highly underexpanded jets.

While these compressibility effects are of prior importance to correctly predict the far field, the results obtained presently prove that their influence remains marginal within the near field. As a consequence, one can assume that the peculiar turbulent mixing within the subsonic transitional zone downstream of the Mach disk is mainly piloted by the strong curvature effects encountered.

## 7. CONCLUSIONS AND PERSPECTIVES

The mixed cell-vertex finite-volume/finite-element method implemented into the CFD code N3Snatur has been coupled with an anisotropic mesh adaptation algorithm to simulate the complex mean structure of highly underexpanded turbulent jets. The various numerical difficulties, encountered when simplified and reduced numerical domains are used, have been described and related to the peculiarities of the near field of the structure of these jets. An overall strategy has thus been suggested to overcome these. It consists in iteratively readapting a 'core grid' to progressively improve the numerical accuracy within the near field and to surround this 'core grid' at each step of the simulation by a strongly coarsened 'buffer grid' in order to naturally dissipate the spurious reflected numerical waves. The influence of such a 'buffer grid' and that of the simplified nozzle geometry on the jet solution remains marginal in the field of interest. Thus, by prescribing a reasonable number of nodes and by using a sufficiently robust hyperbolic solver, this strategy can rapidly lead to correctly converged solutions which yield qualitatively correct jet features over a wide range of NPR. To the authors' knowledge, this is the first time such numerical results obtained for NPR greater than 5 are compared not only with experimental axial evolution but also for the whole near field. Given the simplicity of the models used, the highly underexpanded jet solutions obtained are promising. The main features of the mean complex jet structure are correctly reproduced up to the highest level of NPR simulated while the remaining inaccuracy can be clearly related to two main origins. Firstly, Roe's scheme induces an excessive numerical diffusion within the strong expansion zone so that a new compromise has to be found between robustness and accuracy by implementing and testing more sophisticated hyperbolic solvers for high NPR. Secondly, the results obtained show that the compressibility effects, commonly used to model such flows, only play a minor role in the near field in comparison with the strong curvature effects encountered at the jet boundary near the nozzle or just downstream of the Mach disk. In order to continue to optimize the accuracy/cost ratio of the simulations, improvements in the accuracy of the potential core length prediction may be expected, in particular, by testing adapted non-linear closures of the Reynolds stress tensor components. Preliminary tests have been performed to combine such closures (in particular based on the non-linear algebraic stress model of Shih *et al.* [40]) with the required compressibility corrections required for the far field. Unfortunately, the current modeling appears to make the numerical method unstable, even for reduced CFL numbers. Further works will consist in determining among the available non-linear



DOI: 10.1002/fld

models available, whether adequate limiting functions may be used for the various terms of the transport equations of kinetic turbulent energy and turbulent dissipation in order to make such non-linear closures efficiently useable in the framework of the simulation of highly underexpanded jets.

## NOMENCLATURE

| | |
|---|---|
| $a_i$ | initial angle between the jet boundary and the axis |
| $a_r$ | angle between the reflected shock and the axis |
| $C_i$ | control volume around node $i$ |
| $D_e$ | nozzle diameter |
| $\boldsymbol{D}_r$ | radial diffusive flux vector |
| $\boldsymbol{D}_x$ | longitudinal diffusive flux vector |
| $D_{\mathrm{dm}}$ | Mach disk diameter |
| $E$ | total energy |
| $\boldsymbol{F}_r$ | radial convective flux vector |
| $\boldsymbol{F}_x$ | longitudinal convective flux vector |
| $G$ | enthalpic production |
| $k$ | turbulent kinetic energy |
| NPR | nozzle pressure ratio |
| $D_k$ | diffusion of turbulent kinetic energy |
| $M$ | Mach number |
| $M_{\mathrm{t}}$ | turbulent Mach number |
| $P_k$ | production of turbulent kinetic energy |
| $p$ | pressure |
| $\boldsymbol{S}_r$ | radial source vector |
| $\boldsymbol{S}_x$ | longitudinal source vector |
| $\boldsymbol{U}$ | vector of conservative variables |
| $\boldsymbol{U}_{ij}$ | state vector of conservative variables on the left of $\Gamma_{ij}$ |
| $\boldsymbol{U}_{ji}$ | state vector of conservative variables on the right of $\Gamma_{ij}$ |
| $v_r$ | radial velocity component |
| $v_x$ | longitudinal velocity component |
| $v_{xe}$ | longitudinal velocity component at the nozzle exit |
| $v_\theta$ | orthoradial velocity component |
| $X_{\mathrm{dm}}$ | position of the Mach disk from the nozzle exit |
| $\varepsilon_{\mathrm{c}}$ | dilatational dissipation rate of the turbulent kinetic energy |
| $\varepsilon_{\mathrm{s}}$ | solenoidal dissipation rate of the turbulent kinetic energy |
| $\rho$ | density |
| $\gamma$ | ratio of heat capacities |
| $\mu$ | molecular viscosity |
| $\mu_{\mathrm{t}}$ | coefficient of turbulent viscosity |
| $\Pi_{\mathrm{d}}$ | pressure dilatation term |
| $\Gamma_i$ | boundary of control volume $C_i$ |
| $\Gamma_{ij}$ | boundary between control volumes $C_i$ and $C_j$ |



DOI: 10.1002/fld

ACKNOWLEDGEMENTS

This paper is the result of G. Lehnasch's doctoral thesis carried out at Laboratoire de Combustion et de Détonique, CNRS, Poitiers (France) under the supervision of P. Bruel. The authors wish to thank Drs Yüceïl and Ötügen for the near-field Schlieren visualization of a highly underexpanded jet at NPR = 15.53 they kindly provided.

REFERENCES

1. Chen K, Yao YL, Modi V. Gas dynamic effects on laser cut quality. *Journal of Manufacturing Processes* 2001 **3**(1):38–49.
2. Wilkinson MA, Tester JW. Computational modeling of the gas-phase transport phenomena during flame-jet thermal spallation drilling. *International Journal of Heat and Mass Transfer* 1993; **36**(14):3459–3475.
3. Oberkampf WL, Talpallikar M. Analysis of a high-velocity oxygen fuel (HVOF) thermal spray torch, Part 1: numerical Formulation. *Journal of Thermal Spray Technology* 1996; **5**(1):53–61.
4. Panda J. An experimental investigation of screech noise generation. *Journal of Fluid Mechanics* 1999; **378**:71–96.
5. Avital G, Cohen Y, Gamss L, Kanelbaum Y, Macales J, Trieman B, Yaniv S, Levy M, Stricker J, Sternlieb A. Experimental and computational study of infrared emission from underexpanded rocket exhaust plumes. *Journal of Thermophysics and Heat Transfer* 2001; **15**(4):377–383.
6. Ashkenas H, Sherman FS. The structure and utilization of supersonic free jets in low density wind tunnel. In *Advances in Applied Mechanics—Rarefied Gas Dynamics*. Academic Press: New York, 1965; 84–105.
7. Ewan BCR, Moodie K. Structure and velocity measurements in underexpanded jets. *Combustion Science and Technology* 1986; **45**(5):275–288.
8. Antsupov AV. Properties of underexpanded and overexpanded supersonic gas jets. *Soviet Physics and Technical Physics* 1974; **19**(2):234–238.
9. Glotov GF. Local subsonic zones in supersonic jet flows. *Fluid Dynamics* 1998; **33**(1):117–123.
10. Love ES, Grigsby CE, Lee LP. Experimental and theoretical studies of axisymmetric free jets. *Technical Report R-6*, Langley Research Center, Langley Field, VA, 1959.
11. Krothapalli A, Strykowski PJ, King CJ. Origin of streamwise vortices in supersonic jets. *AIAA Journal* 1998; **36**(5):869–872.
12. Alvi FS, Ladd JA, Bower WW. Experimental and computational investigation of supersonic impinging jets. *AIAA Journal* 2002; **40**(4):599–609.
13. Dash SM, Wolf DE. Interactive phenomena in supersonic jet mixing problems, Part 1: phenomenology and numerical modeling techniques. *AIAA Journal* 1984; **22**(7):905–913.
14. Dash SM, Wolf DE. Interactive phenomena in supersonic jet mixing problems, Part 2: numerical studies. *AIAA Journal* 1984; **22**(10):1395–1404.
15. Chuech SG, Lai MC, Faeth GM. Structure of turbulent sonic underexpanded free jets. *AIAA Journal* 1989; **27**(5):549–559.
16. Cumber PS, Fairweather M, Falle SAEG, Giddings JR. Predictions of the structure of turbulent, moderately underexpanded jets. *AIAA Journal* 1994; **116**:707–713.
17. Cumber PS, Fairweather M, Falle SAEG, Giddings JR. Predictions of the structure of turbulent, highly underexpanded jets. *AIAA Journal* 1995; **117**:599–604.
18. Sarkar S, Erlebach G, Hussaini MY, Kreiss HO. The analysis and modelling of dilatational terms in compressible turbulence. *Journal of Fluid Mechanics* 1991; **227**:473–493.
19. Birkby P, Page GJ. Numerical predictions of turbulent underexpanded sonic jets using a pressure based methodology. *Journal of Aerospace Engineering* 2001; **215**(3):165–173.
20. Abdol-Hamid KS, Wilmoth RG. Multiscale turbulence effects in underexpanded supersonic jets. *AIAA 19th Fluid Dynamics*, *Plasma Dynamics and Lasers Conference*, *AIAA 87-1377*, Honolulu, HI, 1987.
21. Prudhomme SM, Haj-Hariri H. Investigation of supersonic underexpanded jets using adaptative unstructured finite elements. *Finite Elements in Analysis and Design* 1994; **17**(1):21–40.
22. Berzins M, Fairlie R, Pennington SV, Ware JM, Scales LE. Sprint2D: adaptive software for PDEs. *ACM Transactions on Mathematical Software* (*TOMS*) 1998; **24**(4):475–499.
23. Jones WP, Launder BE. The prediction of laminarization with a two-equation model of turbulence. *International Journal of Heat and Mass Transfer* 1972; **15**:301–314.



DOI: 10.1002/fld

24. Shyy W, Krishnamurty VS. Compressibility effects in modeling complex turbulent flows. *Progress in Aerospace Sciences* 1997; **33**(9):587–645.
25. Karmed D, Lahjaily H, Bruel P, Champion M. Influence of the turbulent Damköhler number on the structure of premixed flames in a stagnation flow. *Combustion Science and Technology* 1996; **113–114**:351–365.
26. Bailly C, Lafon P, Candel S. Subsonic and supersonic jet noise predictions from statistical source models. *AIAA Journal* 1997; **35**(11):1688–1696.
27. Zeman O. Dilatation dissipation: the concept and application in modeling compressible mixing layers. *Physics of Fluids A* 1990; **2**(2):178–188.
28. Martin R. *Projet N3S-NATUR*, *V1.4*, *Manuel Théorique*, Software Package, Simulog, France, 2001.
29. Van Leer B. Flux vector splitting for the Euler equations. *Proceedings of the 8th International Conference on Numerical Methods in Fluid Dynamics*. Springer: Berlin, 1982; 507–512.
30. Roe PL. Approximate Riemann solvers, parameter vector and difference schemes. *Journal of Computational Physics* 1981; **43**:357–372.
31. Harten A. High resolution schemes for hyperbolic conservation laws. *Journal of Computational Physics* 1983; **49**:357–393.
32. Obayashi S, Gavali S. Three dimensional simulation of underexpanded plumes using upwind algorithms. *Proceedings of the Conference Supercomputing 88*, Science and Applications, vol. II. Orlando, FL, U.S.A., 1988; 25–33.
33. Satyanarayana M, Balakrishnan N. Adaptive unstructured mesh supersonic jet calculation using AFVS scheme. *Third Asian Computational Fluid Dynamics Conference*, vol. 2. Bangalore, 1998; 378–383.
34. Lehnasch G. Contribution à l'Etude Numérique des Jets Supersoniques Sous-Détendus. *Ph.D. Thesis*, Université de Poitiers et ENSMA, France, 2005.
35. Dolejší V. Anisotropic mesh adaptation technique for finite volume and finite element methods on triangular meshes. *Computing and Visualisation in Science* 1998; **1**(3):165–178.
36. Kolms A. *Computing Unstructured Finite Element Grids on Free-form CAD Surfaces*. ISBN: 3-86005-395-7. Springer: Berlin, 2003; 93–100.
37. Seiner JM, McLaughlin DK, Liu CH. Supersonic jet noise generated by large-scale instabilities. *NASA Technical Paper No. 2072*, 1982.
38. Yüceïl KB, Ötügen MV, Arik E. Underexpanded sonic jets: a PIV study. *Tenth International Symposium on Applications of Laser Techniques to Fluid Mechanics*, Lisbon, Portugal, July 2000.
39. Yüceïl KB, Ötügen MV, Arik E. Interferometric Rayleigh scattering and PIV measurements in the near field of underexpanded sonic jets. *Forty-first Aerospace Sciences Meeting and Exhibit*, *AIAA Paper No. 2003-917*, Reno, Nevada, 2003.
40. Shih TH, Zhu J, Lumley JL. A realizable Reynolds stress algebraic equation model. *NASA TM-105993*, 1993.



DOI: 10.1002/fld